The water vapor self-continuum absorption at 8.45 μm by Optical Feedback Cavity Ring Down Spectroscopy

Quentin Fournier, Samir Kassi, Didier Mondelain, Hélène Fleurbaey, Robert Georges, Alain Campargue

The water vapor self-continuum absorption at 8.45 µm by Optical Feedback Cavity Ring Down Spectroscopy

Q. Fournier[1], S. Kassi[1], D. Mondelain[1], H. Fleurbaey[1], R. Georges[2], A. Campargue[1], *

[1] *Univ. Grenoble Alpes, CNRS, LIPhy, Grenoble, France*
[2] *Univ. Rennes, IPR, Rennes, France*

Friday, 30 November 2023

Key words
Water vapor; continuum absorption; MT_CKD model; CRDS; optical feedback; transparency window

*Corresponding author: Alain Campargue (alain.campargue@univ-grenoble-alpes.fr)

Highlights

- An Optical Feedback Cavity Ring Down Spectrometer (OF-CRDS) is developed at 8.45 µm.
- Water self-continuum cross-sections at 1185 cm^{-1} are measured between 296 to 308 K
- Our cross-section value is found about 20% smaller than the MT_CKD_4.1 value.
- Available measurements in the 10 µm window seem to indicate that the MT_CKD_4.1 temperature dependence is overestimated

Abstract

The accurate knowledge of the water vapor absorption in the 10 µm atmospheric window is of strong importance because this spectral range coincides with the maximum black body emission of Earth. Presently, the water vapor self-continuum is measured at the 1185 cm^{-1} (8.45 µm) spectral point, located in the most transparent interval of the 10 µm window. Measurements are performed at four temperatures ranging from 296 to 308 K using a newly developed Optical Feedback Cavity Ring Down Spectrometer (OF-CRDS). Self-continuum cross-sections, C_S, are derived from the pressure dependence of the absorption during pressure ramps of pure water vapor up to 18 mbar. From the quadratic pressure dependence observed for the absorption coefficient at each temperature, we derived the value of the cross-section (C_s=0.996(12)×10^{-22} $cm^2 molecule^{-1} atm^{-1}$ at 296 K) and its temperature dependence. These results are discussed in relation with previous literature measurements available in the 10 µm window. Our cross-section is found about 20% smaller than the MT_CKD_4.1 value and the available experimental works seem to indicate that the MT_CKD_4.1 temperature dependence is overestimated.

1. Introduction

Earth receives most of its energy from solar radiation. Visible light (corresponding to the maximum emission of the sun's black body) accounts for 40% of the energy received, 50% for the near infrared and 10% for the ultraviolet. About 20% of the incoming radiation is absorbed by the greenhouse gases, mostly by water vapor, but a small amount escapes to space through transparency windows generally coinciding with the regions of low absorption of the water molecule [1].

Water vapor absorption results from the contributions of the water local monomer lines (WML) due to sharp rovibrational transitions, and of a smoother absorption continuum slowly varying with frequency. In our atmosphere, the water vapor continuum is the sum of the self-continuum, related to the interaction between water molecules, and the foreign-continuum, due to interaction of water vapor with other atmospheric molecules, mostly molecular nitrogen and oxygen. Within the transparency windows, the relative contribution of the total water vapor continuum to the atmospheric absorption is much higher than in the band regions, which makes its characterization particularly important. As a result of the equilibrium between the absorption of solar absorption and thermal emission, Earth has an average temperature of 290 K corresponding to a maximum black body emission around 10 µm. The spectral coincidence of the strong black body emission of our planet with the 10 µm atmospheric window makes the accurate knowledge of the water vapor continuum of particular importance in that region, with a direct impact on the Earth's radiation balance [2].

Despite this strong impact, a limited number of studies has been devoted to the quantitative measurements of the absorption self-continuum of water vapor in the 10 µm transparency window (see [3] for a review of the laboratory measurements before 1990). Notable studies include *(i)* the pioneer investigation by Burch and Alt in 1984 using a grating spectrograph and an original optical configuration aiming to minimize the spectra baseline drifts [4], *(ii)* measurements performed at NIST by Baranov et al. using Fourier transform spectroscopy (FTS) with a 100 m pathlength between 311 and 363 K [5], *(iii)* the determination by Cormier et al. of the self-continuum (and N_2-foreign) cross-sections by cavity ring down spectroscopy (CRDS) at 944 cm^{-1} (10.6 µm) for several temperatures in the 270–315 K range [6]. Together with atmospheric measurements, these laboratory results were used to adjust the MT_CKD self-continuum model in the 10 µm window (the MT_CKD semi-empirical model, now included in the HITRAN database [7] is the standard model implemented in atmospheric radiative transfer codes, to account for the water vapor absorption continuum [6, 7, 8]). Nevertheless, due to a dispersion of about 20 % between the different experimental sources, new independent measurements appear to be highly suitable for validation tests of the current MT_CKD model and for modeling the water vapor absorption in the 10 µm window with an accuracy at a level of a few %.

2. OF-CRDS measurements

2.1. Experimental setup

Measurements were performed by cavity ring down spectroscopy [11] (CRDS) using a newly developed spectrometer relying on optical feedback to enhance resonant cavity injection. Basically, CRDS measurement consists in injecting a bunch of photons inside a high finesse cavity, filled with an absorber to measure the photon lifetime τ, which accounts for the various optical losses (mirror losses, sample absorption, Rayleigh scattering, etc…). Technically, after a given level of signal is detected by the cavity transmission photodiode, the laser is switched off and an exponential decay is observed from which the ring down (RD) time, τ, and corresponding loss rate, $1/c\tau$, are derived. By difference with the loss rate obtained with the evacuated cavity, $1/c\tau_0$, the absorption value $\alpha(\nu)$ of the intracavity absorber, is derived:

$$\alpha(\upsilon) = \frac{1}{c}\left(\frac{1}{\tau(\upsilon)} - \frac{1}{\tau_0(\upsilon)}\right) \quad (1)$$

where ν is the laser emission frequency, and c the speed of light. The ultimate sensitivity of the measurement is directly related to the number of photons collected on the photodetector, therefore to the number of photons injected into the optical resonator. In the present system, the empty cavity RD time is about 13 µs, which corresponds to a mirror reflectivity of 99.987%, *i.e.* to a cavity mode width of 10 kHz. The 8.45 µm Quantum Cascade Laser (QCL, Alpes Laser HHL-1083) used in this study presents a linewidth of a few MHz, for a maximum emitted power of 20 mW. This means that in a traditional CRDS configuration (**Fig. 1**, panel (a)), no more than a hundredth of the laser power would be injected into the cavity. To circumvent that issue, we take advantage of the optical feedback mechanism [11]–[13] that permits the laser emission frequency to be kept in close resonance with the cavity modes, without additional electronics control. As depicted in **Fig. 1**, panel (b), this method has been implemented using a 3-mirror V-shaped optical resonator and extensively used for trace detection [14], spectroscopy [15], including water vapor continuum measurement in the 2.3 µm and 4.0 µm infrared windows [16]–[19]. The V-shaped cavity arrangement with an injection through the folding mirror prevents accidental optical-feedback from a direct reflection on it. Only the resonant cavity photons participate in the feedback mechanism. With a well-chosen distance between the laser and the cavity it is possible to quickly record transmission spectra with minimum electronic control. This approach is the basis of optical feedback–cavity enhanced absorption spectroscopy (OF-CEAS). Nevertheless, it suffers from optical fringes and spectral artefacts due to the use of a 3-mirror resonator, where the folding mirror introduces frequency dependent intra-cavity losses. This is why a two-mirror resonator is preferred in the present work.

As shown in **Fig. 1**, panel (c), it is possible to implement an ECDL-like hybrid setup in which an optical element induces enough feedback (OF1) to narrow the laser and enhance the injection of a

two-mirror CRDS resonator [20]. But in such a case, the laser frequency is determined by the external feedback element distance, with no explicit relation with the optical resonator's frequencies themselves. The laser is sent through an acousto-optic modulator and the back reflection from the optical cavity is strictly avoided using an optical isolator. As a result, the cavity injection remains sub-optimal.

As an alternative, depicted in **Fig. 1**, panel (d), we let the laser frequency be firstly governed by the feedback (OF1 in **Fig. 1**) of the cavity input mirror before the cavity resonating photons (OF2) take over. This means that one cannot introduce any optical isolator or acousto-optic modulator between the laser and the cavity as they would hamper the optical feedback mechanism or induce an optical frequency shift, respectively. Such an arrangement has been already described in the literature [21], [22]. The control of the laser/input mirror distance is finely controlled using a PZT-actuated mirror and the laser/cavity distance is chosen to be twice the cavity length, which is kept fixed. Using an optical etalon to monitor the actual laser frequency, we could observe a two-step regime. First, the laser frequency and linewidth are governed by the distance between the laser and the cavity input mirror M2. When this narrowed emission enters in resonance with the cavity, the resonant photons come back to the laser and initiate a second optical-feedback action in competition with the former. Then we observe transmission features like traditional OF-CEAS ones if the laser current is swept. It indicates that the laser is optically locked to the cavity mode and slowly explores the top of the transmission as the current is tuned. This considerable decrease of the current tuning sensitivity is typical of the optical feedback from the resonator [12]. This confirms that the laser emission frequency is imposed by the optical cavity and therefore that the injection efficiency is optimal.

Our detailed setup is described in **Fig. 2**. The laser emission is split in two arms with a beam splitter (20% reflection). The transmitted part is injected into a ZnSe low-finesse optical etalon, whose reflection is detected using a liquid-nitrogen-cooled photoconductive Mercury Cadmium Telluride detector (MCT, J15D16, Teledyne Judson). A quasi-sinusoidal transmission as a function of the laser current is expected in absence of optical feedback, while steps appear when the laser experiences optical feedback from static elements (see **Fig. 3** top panel). This arm is thus used to characterize the laser behaviour and linearize the spectra. The reflected part is sent into the cavity ring down resonator. A pair of germanium lenses allow for a precise mode-matching between the laser beam and the TEM_{00} mode of the resonator. The cavity transmission is recorded using a liquid-nitrogen-cooled photovoltaic MCT detector (J19D12, Teledyne Judson). The laser is powered using a homemade current card, and temperature regulated using a commercial controller (TED 4015, Thorlabs). Both current and temperature are computer controlled. The etalon and cavity signals are recorded using two acquisition cards (National Instrument). The gold mirror controlling the laser-cavity distance is mounted on a

piezoelectric actuator which is driven by a triangular voltage to initiate optical feedback with the CRD cavity.

In the absence of an acousto-optic modulator, the RD events are initiated by switching off the laser current for a few µs. Exponential decays are then observed and fitted. By hopping the laser over cavity modes, CRDS spectra can be recorded. A sample raw spectrum is shown in **Fig. 3** along with the etalon trace which was used to linearize the frequency axis. The spectral step resolution is given by the free spectral range of the resonator (about 300 MHz with the used 50 cm long cell) and the instrument line shape is determined by the cavity linewidth (about 10 kHz). A typical transmission trace is shown in the right top panel in **Fig. 3**. It is similar to traditional OF-CEAS ones as the laser current is swept.

The cell pressure is monitored with a pressure transducer (MKS Baratron, 20 Torr range, 0.25% of accuracy at full scale) and software regulated by acting on an upstream electro-valve while a manual needle valve, installed downstream, permits to limit the gas flow. The temperature of the cell was continuously monitored using a pair of temperature probes (PT 1000 with 0.1 K accuracy) installed on the cell extremities. The sample temperature could be changed using a heating ribbon wrapped around the cell. To reach different temperatures, the voltage applied to the ribbon was varied to different fixed values, and the recording started once a steady state was reached.

The sample preparation is a key point for the self-continuum measurement. A glass tank was filled with about 10 ml of liquid water sample (commercial demineralized water). The sample was then briefly pumped down to its boiling point in order to quickly extract part of the dissolved gases. Then the sample was cooled down to liquid nitrogen temperature, while pumping on it with a turbo molecular pump to extract the remaining dissolved gases. Once totally frozen, the temperature was raised up to room temperature and the sucking power reduced but not interrupted. We found that a continuous flow had to be kept to avoid any contamination during measurement. Therefore, only part of the water vapor flow was derived towards the measurement cell.

2.2. Spectra acquisition

The spectra were acquired using the OF-CRDS technique described above. The laser frequency was tuned by varying its chip temperature from 8°C to 32°C corresponding to a scanning range of about 1.8 cm^{-1}. The laser is multimode or stops lasing at lower or higher temperature, respectively.

Because the laser current is interrupted during the RD event, the laser does not lock systematically on the same modes after the current is switched on again. The ZnSe etalon trace, which is recorded synchronously with the spectrum, *i.e.* a few µs before the RD event occurs, permits to non-ambiguous association of the RD event to a specific cavity longitudinal mode (**Fig. 3**). During the broadband scans, the temperature is slowly and continuously swept and the data collected on the fly. The spectrum is reconstructed offline using a Python based post-treatment procedure. Each spectral point is typically the

192 average of about 10 RD events occurring at the same optical frequency which corresponds to a given
193 cavity mode. The minimum detectable absorption coefficient is 10^{-8} cm^{-1}.

194 Following this method, we recorded a water vapor absorption spectrum at 9 mbar shown in **Fig.**
195 **4** to determine the accessible laser frequency range. Such a full range spectrum is obtained within
196 typically 20 minutes. By comparison with a simulation based on HITRAN parameters, a correspondence
197 between laser temperature and frequency could be determined with a 0.01 cm^{-1} accuracy. In addition to
198 the monomer lines, the spectrum reveals a continuum contribution.

199
200
201 Such a spectrum also permits to check the presence of contaminating gas presenting absorption
202 lines in the region. This is the case for CH_4 and N_2O, that we could clearly identify with insufficiently
203 purified water samples and stainless steel rather than glass tanks.

204 In **Fig. 5**, the pressure dependence of the spectra is illustrated by the evolution of the baseline in
205 spectra recorded at 0, 4.5, 9 and 18 mbar. Note that the baseline evolution of the different spectra with
206 respect to that at zero pressure increases quadratically with pressure due to the combined effects of self-
207 continuum and (to a lesser extent) of the cumulative contribution of the monomer line profiles truncated
208 at ±25 cm^{-1} from their center. The spectrum at 0 mbar corresponds to the reflectivity curve of the cavity
209 mirrors, which is centered at 1250 cm^{-1}.

210 The acquisition time of a single spectrum is relatively long (20 minutes approximately) which
211 makes the measurement of the self-continuum sensitive to long-term instrumental changes (temperature
212 variations, instrumental drifts, etc...). In order to minimize experimental biases, we preferred to derive
213 the absorption continuum from the variation of the OF-CRDS loss rate during pressure ramps at a fixed
214 spectral point. The typical duration of a pressure ramp from 0 to 15 mbar is shorter than 2 minutes. The
215 spectral point at 1184.94 cm^{-1} (dotted line in **Fig. 5**), which minimizes the contribution of the water line
216 profiles, was selected for the self-continuum retrieval.

217
218

219 *2.3. Self-continuum cross-sections*

220 An experimental spectrum of water vapor recorded at 9 mbar and 296 K is shown above, in **Fig.**
221 **4** blue line). The measured experimental absorption is the sum of the water monomer contribution,
222 $\alpha_{WML}(\nu)$, and of the self-continuum contribution, $\alpha_{WCS}(\nu)$:

223 $$\alpha(\nu,T) = \alpha_{WML}(\nu,T) + \alpha_{WCS}(\nu,T) = \alpha_{WML}(\nu,T) + \frac{1}{kT} C_S(\nu,T) P_{H_2O}^2 \quad (2)$$

224 with k the Boltzmann constant, T and P respectively the temperature and pressure of the gas inside the
225 cavity.

226 The self-continuum absorption varies quadratically with the water vapor pressure with a
227 proportionality factor defining the self-continuum cross-section, $C_S(\nu,T)$, expressed in $cm^2 molecule^-$

[1]atm^{-1}. The line contribution, $\alpha_{WML}(\nu)$, (grey background in **Fig. 4)** is obtained as a spectrum simulation using the HITRAN2020 line parameters [7] and a Voigt profile with the standard ±25 cm^{-1} wing cut-off from the line centre without including the pedestal [19].

The water vapor absorption at the selected spectral point was monitored during increasing and decreasing pressure ramps between 0 and 18 mbar (corresponding to 65 % of the vapor pressure of water). The duration of the ramp was varied from 1 to 2 minutes, without any significant effect on the absorption signal. The measured signal was also found to be unaffected by a change of the flow of water vapor injected in the cell. The pressure dependence of the OF-CRDS loss rate at 1184.94 cm^{-1} is displayed in **Fig. 6**. A purely quadratic pressure dependence is observed with no significant deviation between the data obtained during the increasing and decreasing pressure ramps (both measurements are superimposed on the graph). As a check of the absence of bias due to mechanical effects related to the gas injection, we have monitored the OF-CRDS signal during pressure ramps using argon instead of water vapor. Argon is not absorbing and only induces negligible Rayleigh scattering losses. The results (included in **Fig. 6**) illustrate the absence of significant variation of the loss rate when argon is injected.

Pressure ramps were performed at four temperature values: 296.3, 300.7, 304.3 and 307.9 K. The pressure dependences included in **Fig. 6** illustrate the decrease of the self-continuum absorption with temperature. The cell temperature was changed gradually by heating the cavity with a rheostat and heating cable. As the temperature was not controlled, the temperature variation was chosen to be extremely slow to allow the system to stabilize at different temperature levels. Two Pt1000 thermistors, placed on either side of the cavity, revealed the existence of a temperature gradient between the inlet and outlet. This gradient increases with temperature leading to error bars increasing from ±0.1 K at room temperature to ±1.7 K at 307.9 K.

We have included in **Fig. 6** (orange line) the contribution of the monomer lines, α_{WML} (ν=1184.94 cm^{-1}), calculated at each temperature step from spectra simulations based on the HITRAN2020 database [7]. The monomer contribution is almost the same at all the temperature values. Its pressure dependence, also quadratic, corresponds to 11% of the measured total absorption at 296 K (this percentage increases to 13% at 307.9 K).

2.4. Results

The number of ramp acquisitions at the four measurement temperatures varies between 9 and 20 (see **Table. 1**). For each ramp acquisition, the monomer contribution was subtracted and the self-continuum cross-section, $C_S(\nu, T)$, was derived from the slope of the curves presented in **Fig. 6** (following Eq. 2). The obtained cross-section values are listed in **Table. 1**.

Error bars on the self-continuum cross-sections were derived by propagating the various sources of uncertainty identified. From Eq. 2, we see that the retrieved C_s values depend on the difference between the total absorption and the contribution of the local water monomer. The uncertainty of this latter contribution is calculated from the uncertainty reported in the HITRAN database for the line intensities and self-broadening coefficients (see [19] for more details). The potential impact of additional absorption due to pollutant species observed when a stainless steel tank was used (and which disappeared when using a glass tank), is taken into account at 1184.94 cm^{-1} by considering that the maximum absorption structure of that pollutant is at the noise level. Pressure uncertainty is due to the pressure gauge uncertainty (*i.e.* 0.25% full scale or 0.05 Torr). The uncertainty on temperature corresponds to the temperature sensor uncertainty at 296 K (*i.e.* 0.1K) and to the observed temperature gradients for the higher temperatures. Note that the temperature uncertainty impacts the C_s uncertainty through Eq. 2 and through its temperature dependence. Finally, statistical uncertainty was considered through the standard error of mean of the measured C_s values at a given temperature (this includes temporal variations of the base line). At 296.3 K, uncertainties are mostly due to the uncertainty of the monomer contribution and to the potential absorption of the pollutant species. At higher temperatures, the uncertainties are dominated by the temperature gradient (3% at 307.7 K).

3. Discussion

3.1. Comparison with literature

In the following, the experimental values of literature will be compared with the MT_CKD empirical model. Note that from version V4.1, the MT_CKD $\tilde{C}_s^{MTCKD}(\nu,T)$ values as provided in HITRAN2020 [23] must be multiplied by a radiative term $R(\nu,T)$ such as:

$$C_s(\nu,T) = \tilde{C}_s^{MTCKD}(\nu,T) \times R(\nu,T) \quad (3)$$

where

$$R(\nu,T) = \nu \tanh\left(\frac{hc\nu}{2kT}\right) \quad (4)$$

with ν the wavenumber, h the Planck constant, k the Boltzmann constant. The cross-section values given by the MT_CKD software at any temperature are normalized to the number density at standard conditions (1 atm, 296 K) and should be multiplied by the factor 296/T when expressed in $cm^2molec^{-1}atm^{-1}$ units.

In **Fig. 7**, our cross-section value at 296 K is compared to the current MT_CKD_4.1 values and to the literature values available in the 10 µm region. Our C_s value at 1185 cm^{-1} is found smaller by about 20% compared with the MT_CKD_4.1 model, which is identical to version V3.2 in this region [21]. Previous measurements available in the region are due to *(i)* Burch&Alt who used a grating spectrograph with temperatures ranging from 284 to 430 K [4], *(ii)* Baranov et al. who used an FTS at 311 and 363 K [5], and *(iii)* Cormier et al. by CRDS at 944 cm^{-1} and temperatures ranging between 270 and 315 K [6]. For the sake of comparison, the values of Baranov et al. have been extrapolated to the

296 K reference temperature using the MT_CKD temperature dependence. The MT_CKD model mostly fits with the values of Baranov et al. while the three other experimental sources (Burch&Alt, Cormier et al. and the present work) form a consistent dataset systematically lower by about 20% compared to MT_CKD_4.1.

3.2. Temperature dependence

Fig. 8 shows the variation of $C_s(T)$ (in logarithmic scale) *versus* the reciprocal of the temperature. As evidenced by Burch&Alt, a straight line corresponding to an empirical law of the type $C_s(T_0)\exp[B(1/kT-1/kT_0)]$ is frequently found consistent with the observations and accounts for the strong negative dependence of the self-continuum *versus* temperature. The B parameter can be determined from a statistical fit of the various temperature dependences available in the literature (see **Table 2**). A fit of our $C_s(T)$ values in the 296-308 K interval leads to B= 1282(57) cm^{-1} which is very close to the value derived from Cormier data at 945 cm^{-1}, in the 270-315 K range [1295(23) cm^{-1}]. At 1044 cm^{-1}, a similar fit applied to the values of Baranov et al. between 311 and 363 K yields B= 989(36) cm^{-1}. In Fig. 3 of Ref. [4], Burch&Alt reported C_s values at 284, 296 and 392 K from which we derive quite different B values of 1081 and 1683 cm^{-1} for the 284-296 K and 296-392 K intervals, respectively.

For the four available experimental sources, the experimental data are very well reproduced by the above empirical law with fitted value of B ranging between 980 and 1300 cm^{-1}. This is less the case for the MT_CKD_4.1 temperature dependence for which, at the 1185 cm^{-1} spectral point, we obtain B values of about 1475 and 1990 cm^{-1} around 300 and 400 K, respectively (at the 1000 cm^{-1} spectral point, these values increase up to 1637 and 2216 cm^{-1}, respectively). Thus, the MT_CKD_4.1 decrease of the self-continuum with temperature appears to be larger than measured. Let us note that the fitted values of B of the four experimental works are close to the dissociation energy of the water dimer, D_0= 1144 cm^{-1} [24] (see dashed curve in **Fig. 8**). In the 2.3 µm window [15], the experimental values were also well modeled by the $A\exp(D_0/kT)$ empirical law while in the 1.6 µm window (where the self-continuum is much weaker), the C_s temperature dependence was found less pronounced [25]. The temperature dependence in the 1.25 µm window [26] remains to be determined.

5. Conclusion

We have developed a laser spectrometer at 8.5 µm. It is based on optical feedback from a linear optical cavity onto a QCL laser. So-called optical-feedback cavity-ring-down measurements have been performed with an absorption detection limit of 10^{-8} cm^{-1}. It allowed for the measurement of the self-continuum absorption of water vapor in the 296 to 308 K temperature range, at a spectral point located in the most transparent interval of the 10 µm atmospheric window. Special care was taken to purify the water sample, and measurements were carried out in flow conditions. The derived self cross-section value at 1185 cm^{-1} is consistent with the pioneer measurements by Burch&Alt [4] between 700 and 1060 cm^{-1} and those by Cormier et al. near 944 cm^{-1} [6]. These three sets of measurements are nevertheless about 20% smaller than the cross-section values provided by the current version V4.1 of the MT_CKD model (which coincides with the FTS values of Baranov et al. [5]). Note that independently of the present laboratory measurements, atmospheric data have provided additional evidence that the MT_CKD_4.1 self-continuum has to be decreased in the region [27]. This modification will be taken into account in the next version of the MT_CKD model (V4.2, not yet released). The impact of the resulting higher transparency of the 10 µm window in the radiative transfer modeling of our planet deserves to be quantified as this window corresponds to the maximum black body emission of our planet.

As concerns the temperature dependence of the self-continuum in the region, the available experimental data (**Fig. 8**) seem to indicate that the MT_CKD_4.1 temperature dependence is significantly stronger than measured. This is an important point which should motivate further measurements in the temperature range of our atmosphere.

Acknowledgements:
This work was financially supported by the Agence Nationale de la Recherche (project ANR-20-CE31-0014). Thanks to P. Asselin from MONARIS laboratory (Sorbonne University in Paris) for the loan of MCT detector. Special thanks to the engineer B. Travers for all the support concerning electronics and mechanics development. Valuable exchanges with E. Mlawer (AER) are acknowledged.

Declaration of interests

The authors declare that they have no known competing financial interests or personal relationships that could have appeared to influence the work reported in this paper.

References

[1] G. L. Stephens *et al.*, « An update on Earth's energy balance in light of the latest global observations», *Nature Geosci*, 2012;5(10):691–696, doi: 10.1038/ngeo1580.

[2] D. D. B. Koll and T. W. Cronin, « Earth's outgoing longwave radiation linear due to H_2O greenhouse effect », *Proc Natl Acad Sci U.S.A.*,2018;115(41):10296-10298. doi: 10.1073/pnas.1809868115.

[3] W. B. Grant, « Water vapor absorption coefficients in the 8-1 3-,µm spectral region: a critical review». *Applied Optics*, 1990;29(4): 451-462. doi:10.1364/AO.29.000451

[4] D. E. Burch and R. L. Alt, 'Continuum absorption by H_2O in the 700 – 1200 cm^{-1} and 2400 – 2800 cm^{-1} windows', *Report AFGL-TR-84-0128, Air Force Geophys. Laboratory, Hanscom AFB, MA*, 1984.

[5] Yu. I. Baranov, W. J. Lafferty, Q. Ma, and R. H. Tipping, « Water-vapor continuum absorption in the 800–1250 cm^{-1} spectral region at temperatures from 311 to 363K », *J Quant Spectrosc Radiat Transf*, 2008;109(12-13):2291-2302. doi: 10.1016/j.jqsrt.2008.03.004

[6] J. G. Cormier, J. T. Hodges, and J. R. Drummond, « Infrared water vapor continuum absorption at atmospheric temperatures », *J Chem Phys*, 2005;122(11):114309. doi: 10.1063/1.1862623.

[7] I. E. Gordon *et al.*, « The HITRAN2020 molecular spectroscopic database », *J Quant Spectrosc Radiat Transf*, 2022;277:107949. doi: 10.1016/j.jqsrt.2021.107949.

[8] S. A. Clough, F. X. Kneizys, and R. W. Davies, « Line shape and the water vapor continuum », *Atmos Res*, 1989;23(3-4):229-241. doi: 10.1016/0169-8095(89)90020-3.

[9] E. J. Mlawer, V. H. Payne, J.-L. Moncet, J. S. Delamere, M. J. Alvarado, and D. C. Tobin, « Development and recent evaluation of the MT_CKD model of continuum absorption », *Phil Trans R Soc A*, 2012;370(1968):2520-2556. doi: 10.1098/rsta.2011.0295.

[10] http://rtweb.aer.com/continuum_description.html

[11] J. Morville, D. Romanini, A. A. Kachanov, and M. Chenevier, « Two schemes for trace detection using cavity ringdown spectroscopy », *Appl Phys B*, 2004;78(3–4):465-476. doi: 10.1007/s00340-003-1363-8.

[12] J. Morville, D. Romanini, and E. Kerstel, « Cavity Enhanced Absorption Spectroscopy with Optical Feedback », in *Cavity-Enhanced Spectroscopy and Sensing*, G. Gagliardi et H.-P. Loock, Éd., in Springer Series in Optical Sciences, Springer Berlin Heidelberg, 2014;179:163-209. doi: 10.1007/978-3-642-40003-2_5.

[13] P. Laurent, A. Clairon, and C. Breant, « Frequency noise analysis of optically self-locked diode lasers », *IEEE J Quantum Electron*, 1989;25(6):1131-1142. doi: 10.1109/3.29238.

[14] L. Richard, D. Romanini, and I. Ventrillard, « Nitric Oxide Analysis Down to ppt Levels by Optical-Feedback Cavity-Enhanced Absorption Spectroscopy », *Sensors*, 2018;18(7):1997. doi: 10.3390/s18071997.

[15] J. Chaillot, S. Dasari, H. Fleurbaey, M. Daeron, J. Savarino, and S. Kassi, « High-precision laser spectroscopy of H_2S for simultaneous probing of multiple-sulfur isotopes », *Environ Sci: Adv*, 2023;2(1):78-86. doi: 10.1039/D2VA00104G.

[16] L. Lechevallier, S. Vasilchenko, R. Grilli, D. Mondelain, D. Romanini, and A. Campargue, « The water vapor self-continuum absorption in the infrared atmospheric windows: New laser measurements near 3.3 µm and 2.0 µm », *Atmos Meas Tech* 2018;11:2159–2171. doi:10.5194/amt-11-2159-2018

[17] L. Richard, S. Vasilchenko, D. Mondelain, I. Ventrillard, D. Romanini, and A. Campargue, « Water vapor self-continuum absorption measurements in the 4.0 and 2.1 µm transparency windows », *J Quant Spectrosc Radiat Transf*, 2017;201:171-179. doi: 10.1016/j.jqsrt.2017.06.037.

[18] I. Ventrillard, D. Romanini, D. Mondelain, and A. Campargue, « Accurate measurements and temperature dependence of the water vapor self-continuum absorption in the 2.1 µm atmospheric window », *J Chem Phys*, 2015;143(13):134304. doi: 10.1063/1.4931811.

[19] H. Fleurbaey, R. Grilli, D. Mondelain, and A. Campargue, « Measurements of the water vapor continuum absorption by OFCEAS at 3.50 µm and 2.32 µm », *J Quant Spectrosc Radiat Transf*, 2022;278:108004. doi: 10.1016/j.jqsrt.2021.108004.

[20] P. Čermák, S. Vasilchenko, D. Mondelain, S. Kassi, and A. Campargue, « First laboratory detection of an absorption line of the first overtone electric quadrupolar band of N_2 by CRDS near 2.2 µm », *Chem Phys Lett*, 2017;668:90-94. doi: 10.1016/j.cplett.2016.11.002.

[21] J. Tian, G. Zhao, A. J. Fleisher, W. Ma, and S. Jia, « Optical feedback linear cavity enhanced absorption spectroscopy », *Opt Express*, 2021;29(17):26831. doi: 10.1364/OE.431934.

[22] G. Zhao, J. Tian, J. T. Hodges, and A. J. Fleisher, « Frequency stabilization of a quantum cascade laser by weak resonant feedback from a Fabry-Perot cavity », *Opt Lett*, 2021;46(13):3057. doi: 10.1364/OL.427083.

[23] E. J. Mlawer, K. E. Cady-Pereira, J. Mascio, and I. E. Gordon, « The inclusion of the MT_CKD water vapor continuum model in the HITRAN molecular spectroscopic database », *J Quant Spectrosc Radiat Transf*, 2023;306:108645. doi: 10.1016/j.jqsrt.2023.108645.

[24] E. A. Serov, M. A. Koshelev, T. A. Odintsova, V. V. Parshin, and M. Yu. Tretyakov, « Rotationally resolved water dimer spectra in atmospheric air and pure water vapour in the 188–258 GHz range », *Phys Chem Chem Phys*, 2014;16(47):26221-26233. doi: 10.1039/C4CP03252G.
[25] D. Mondelain, S. Manigand, S. Kassi, and A. Campargue, « Temperature dependence of the water vapor self-continuum by cavity ring-down spectroscopy in the 1.6 µm transparency window », *J Geophys Res Atmos*, 2014;119(9):5625-5639. doi: 10.1002/2013JD021319.
[26] T. A. Odintsova, A. O. Koroleva, A. A. Simonova, A. Campargue, and M. Yu. Tretyakov, « The atmospheric continuum in the "terahertz gap" region (15–700 cm^{-1}): Review of experiments at SOLEIL synchrotron and modeling », *J Mol Spectrosc*, 2022;386:111603. doi: 10.1016/j.jms.2022.111603.
[27] E. Mlawer, 15th ASA-HITRAN conference, Reims (August 2022).

Fig. 1 Schematic of the typical optical arrangement used for (a) a traditional CRDS, (b) classical optical-feedback cavity enhanced absorption spectroscopy (c) CRDS with homemade external cavity diode laser (ECDL) (d) the present optical-feedback cavity ringdown spectrometer. (b) and (d) exploit the contra-propagating photons resonant with a high finesse cavity (OF2). The three-mirror-based V-shape arrangement (b) avoids optical feedback (OF1) from direct reflection on the input mirror M2 but suffers intra-cavity losses arising from this folding mirror M2. The ECDL arrangement (c) uses OF1 to narrow the laser emission width and enhance the cavity injection. The two-mirror linear cavity arrangement (d) avoids unwanted extra intra-cavity losses, but both OF1 and OF2 are in competition. OI: Optical isolator, M: Mirrors, Δφ: Phase control, PD: Photodiode, LAS: Laser.

Fig. 2 Schematic view of the OF-CRDS experimental setup. It includes all the different organs linked to the spectroscopy technique and the management of experimental parameters.
BS: Beam splitter, PZT: Piezoelectric system, MCT: Mercury Cadmium Telluride detector, LAS 1: MIR laser, LAS 2: Alignment NIR laser.

Fig. 3 Top left panel: etalon trace. Bottom left panel: corresponding OF-CRDS spectrum obtained at 200 mbar of ambient air by scanning the laser temperature. The trace of the etalon is recorded at the same time as the RD are acquired. For each scanned cavity mode, we distinguish frequency-separated steps of 300 MHz (on the top, red dot on the etalon trace). The losses are then sorted and averaged (bottom black line). Top right panel: example of an OF-CEAS like mode obtained by scanning the laser current. After the photodiode transmission signal reaches a given level, the laser is switched off and an exponential decay is observed (red dashed line). A RD time is deduced. Bottom right panel: illustration of the laser real frequency behavior while its current is ramped. Two regimes are observed: the laser is sharpened by the OF1, no signal is observed. Then OF2 takes over the laser gets locked to the cavity mode.

Fig. 4 OF-CRDS spectrum of water vapor around 1185 cm^{-1} (P= 9 mbar and T= 296 K) (cyan) compared to a spectrum simulation based on the HITRAN database (grey, line contribution truncated at ±25 cm^{-1} from the line center without including the pedestal). The baseline of the OF-CRDS spectrum corresponds to the cavity loss rate obtained with an evacuated cavity (P= 0 mbar). The self-continuum absorption is obtained as the difference between the OF-CRDS signal and the HITRAN simulation.

Fig. 5 Pure water spectra recorded at room temperature for four pressure values (0 mbar in black, 4.5 mbar in red, 9 mbar in green, 18 mbar in blue). Wavenumber scale has been determined by combining the etalon trace for each absorption point, and by identifying the absorption water lines in HITRAN. The dashed line at 1184.94 cm^{-1} corresponds to the frequency position of the self-continuum cross-section measurement. The spectral resolution is 300 MHz, corresponding to the free spectral range of the cavity.

Fig. 6 Variation of the OF-CRDS loss rate at 1184.94 cm^{-1} during pressure ramps of water vapor. Experimental ramps were performed between 0 and 18 mbar at four different temperatures (296.3, 300.7, 304.3 and 307.9 K).

The loss rate of the evacuated cavity was subtracted from the measured loss rates to get the displayed absorption coefficients. After removal of the monomer contribution (in orange), the different cross-section values, C_S, are obtained from the slope. Argon ramp (cyan circles) is represented to illustrate the fact that there is no significant bias due to mechanical deformations. The minimum detectable absorption coefficient is 10^{-8} cm^{-1}.

Fig. 7 Overview comparison to the MT_CKD_4.1 model [23] of the measurements of the water vapor self-continuum in the 10 µm transparency window: Burch&Alt1986 [4], Cormier2005 [6], Baranov et al. [5] and present work.

Fig. 8 Temperature dependence of the water vapor self-continuum cross-section (C_s) between 270 and 363 K. Orange open squares correspond to the present OF-CRDS results at 1185 cm^{-1} in the 296-308 K range, with their corresponding error bars. The uncertainties on the temperature (related to the temperature gradient) are also shown. The dashed blue curve corresponds to a $Ae^{\frac{D_0}{kT}}$ law where D_0 is the dissociation energy of the water dimer, D_0=1144 cm^{-1} [24]. The MT_CKD_4.1 values are displayed for comparison (red solid curve). The measurements at 1044.5 cm^{-1} by Baranov et al, at 1000 cm^{-1} by Burch&Alt and at 944 cm^{-1} by Cormier et al. are shown for comparison.

Table. 1 Self-continuum cross sections of water vapor measured by OF-CRDS at 1184.94 cm^{-1} between 296 and 308 K.

Temperature (K)	Nb of ramps	C_s (10^{-22} cm^{2}molecule^{-1}atm^{-1})	
		This work	*MT_CKD_4.1*
296.3	20	0.996(12)	1.248
300.7	10	0.895(13)	1.125
304.3	10	0.840(19)	1.034
307.9	9	0.786(27)	0.952

Table 2 **Experimental conditions and corresponding fitted value of the *B* parameter defined in $C_s(T)=C_s(T_0)\exp[B(1/kT-1/kT_0)]$, for the different experimental studies available in the 10 µm window and comparison to the MT_CKD_4.1 temperature dependence.**

Reference	Spectral point (cm^{-1})	*T* range (K)	*B* (cm^{-1}) [a]
Burch&Alt [4]	1000	284 and 296	1081
		296 and 392	1683
Baranov et al [5]	1044	311-363	989(36)
Cormier et al. [6]	945	270-315	1295(23)
This work	1185	296-308	1282(57)
MT_CKD_4.1 [23]	1185	~ 300	1475
		~ 400	1990

Note

[a] The uncertainty values given within parenthesis correspond to the statistical uncertainty. Due to possible correlation between the uncertainties, real error bars are probably significantly larger.

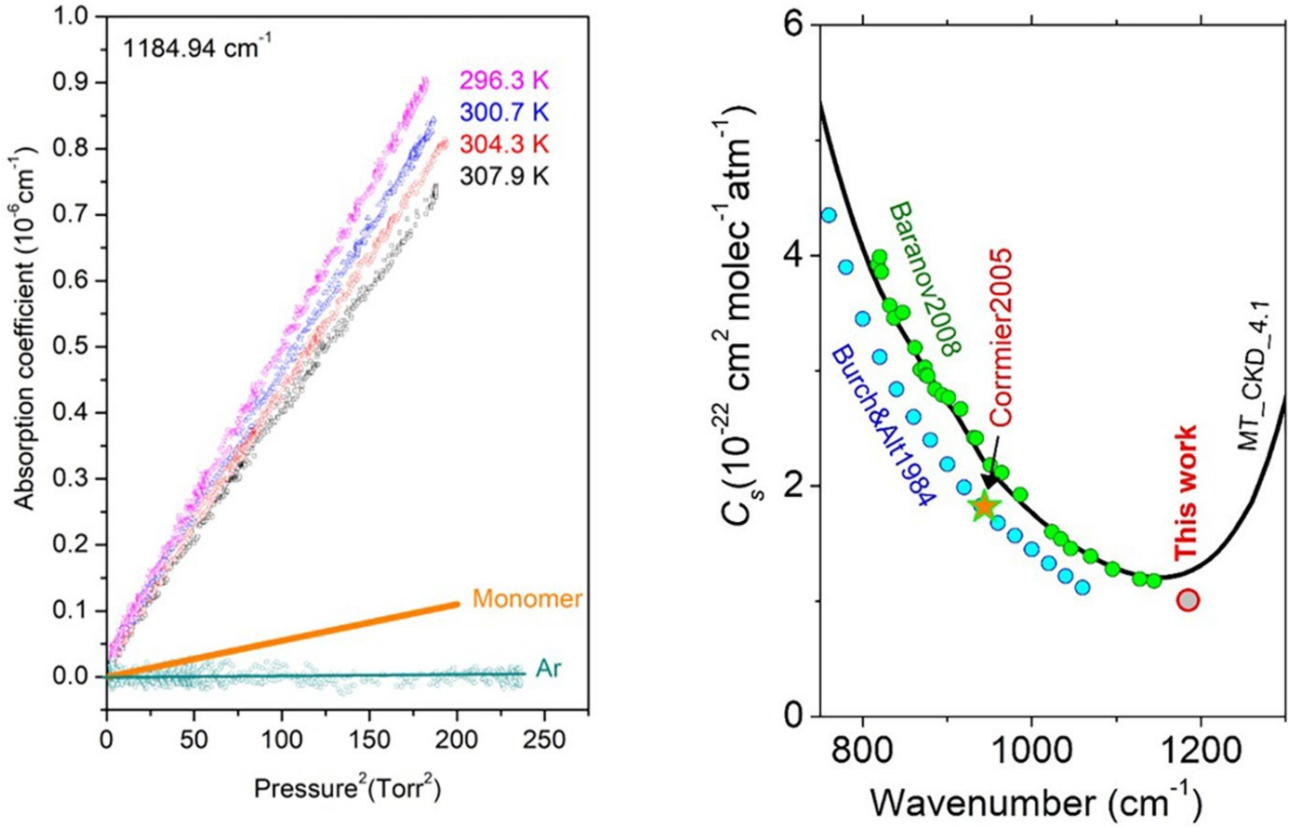

Graphical abstract

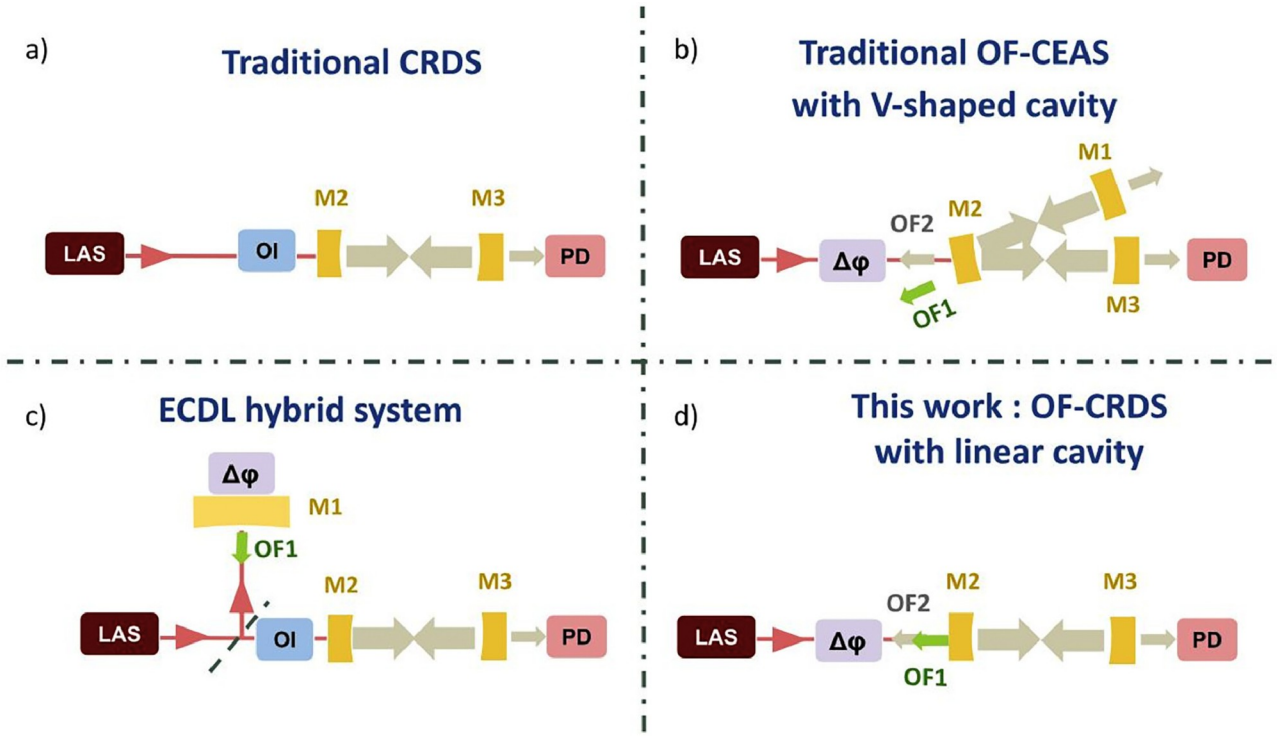

Fig. 1

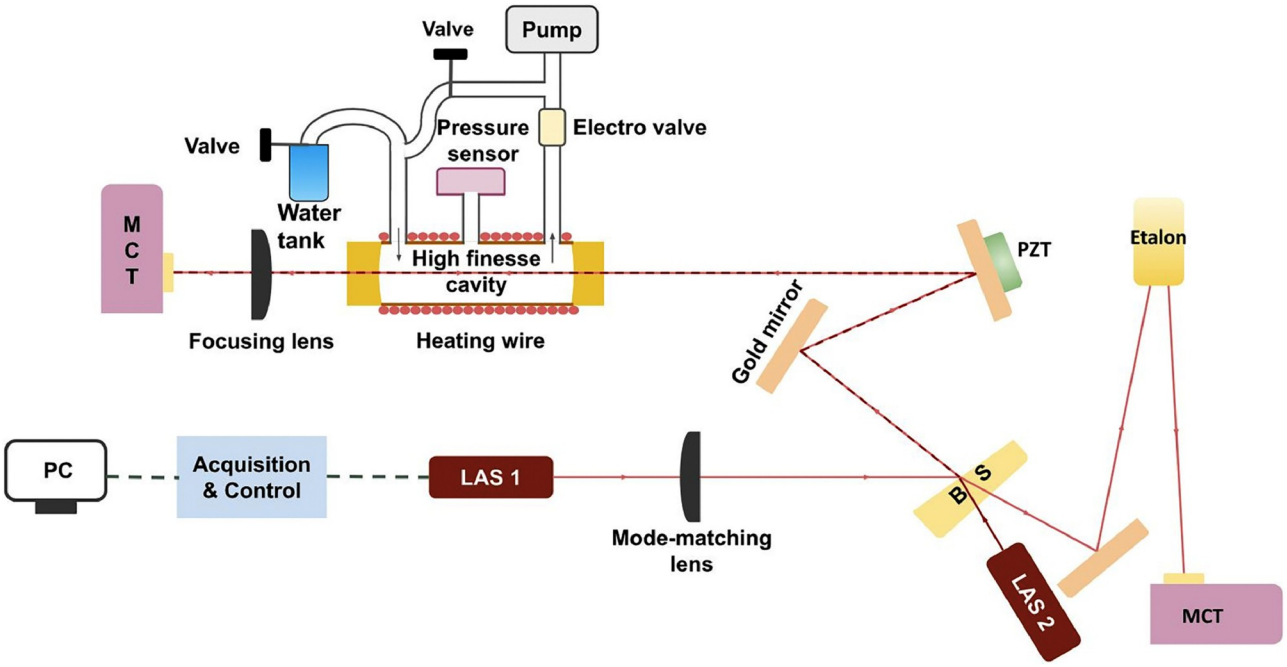

Fig. 2

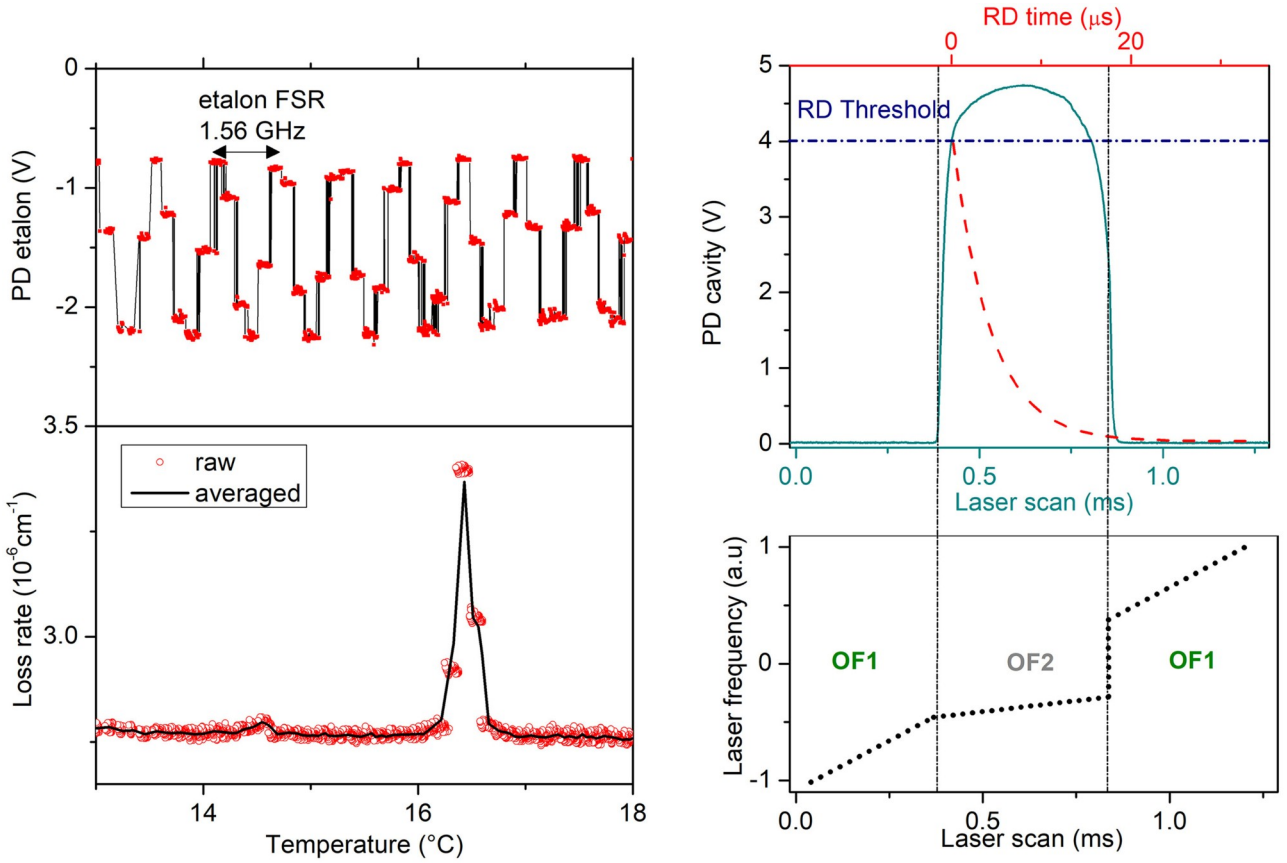

Fig. 3

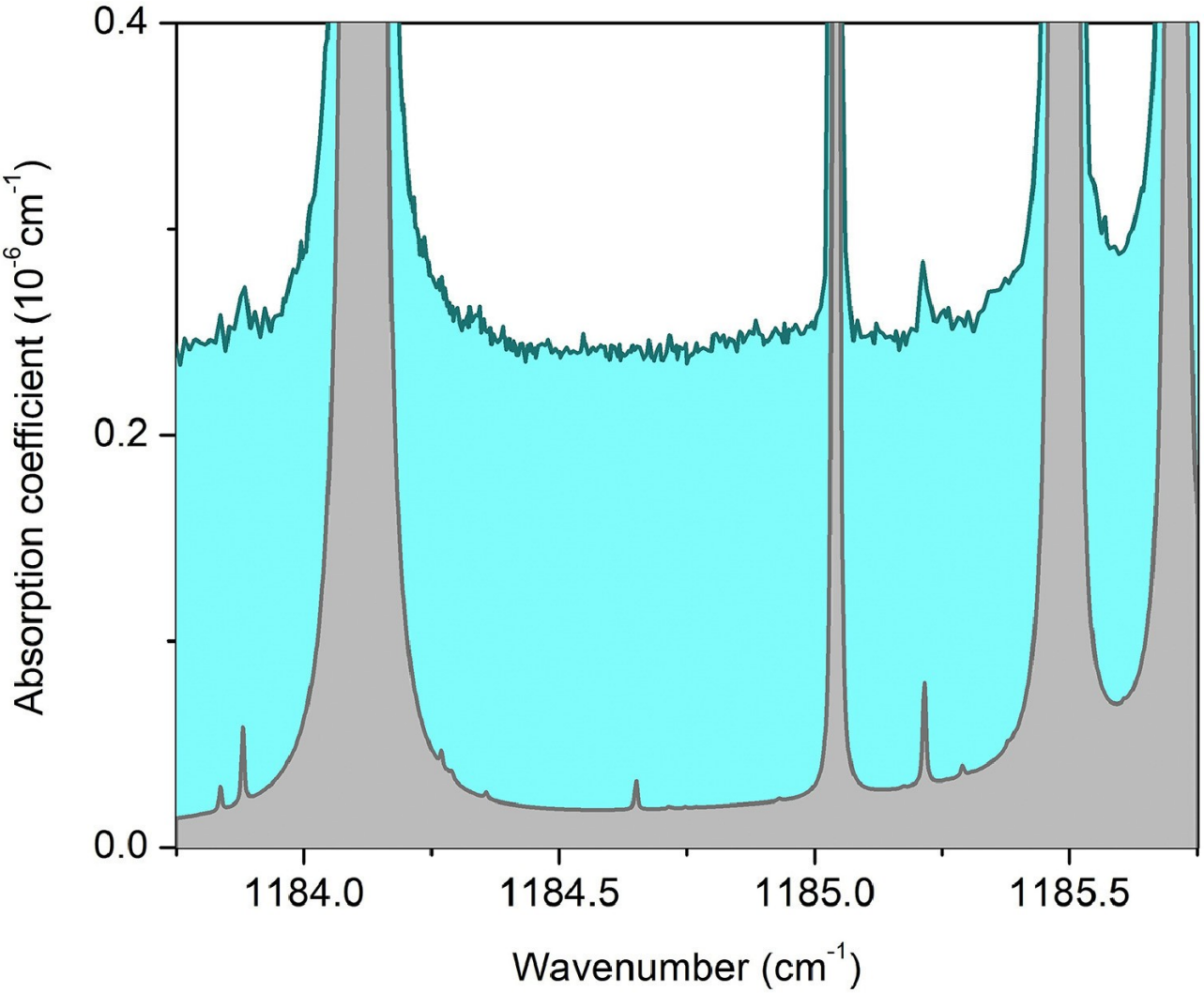

Fig . 4

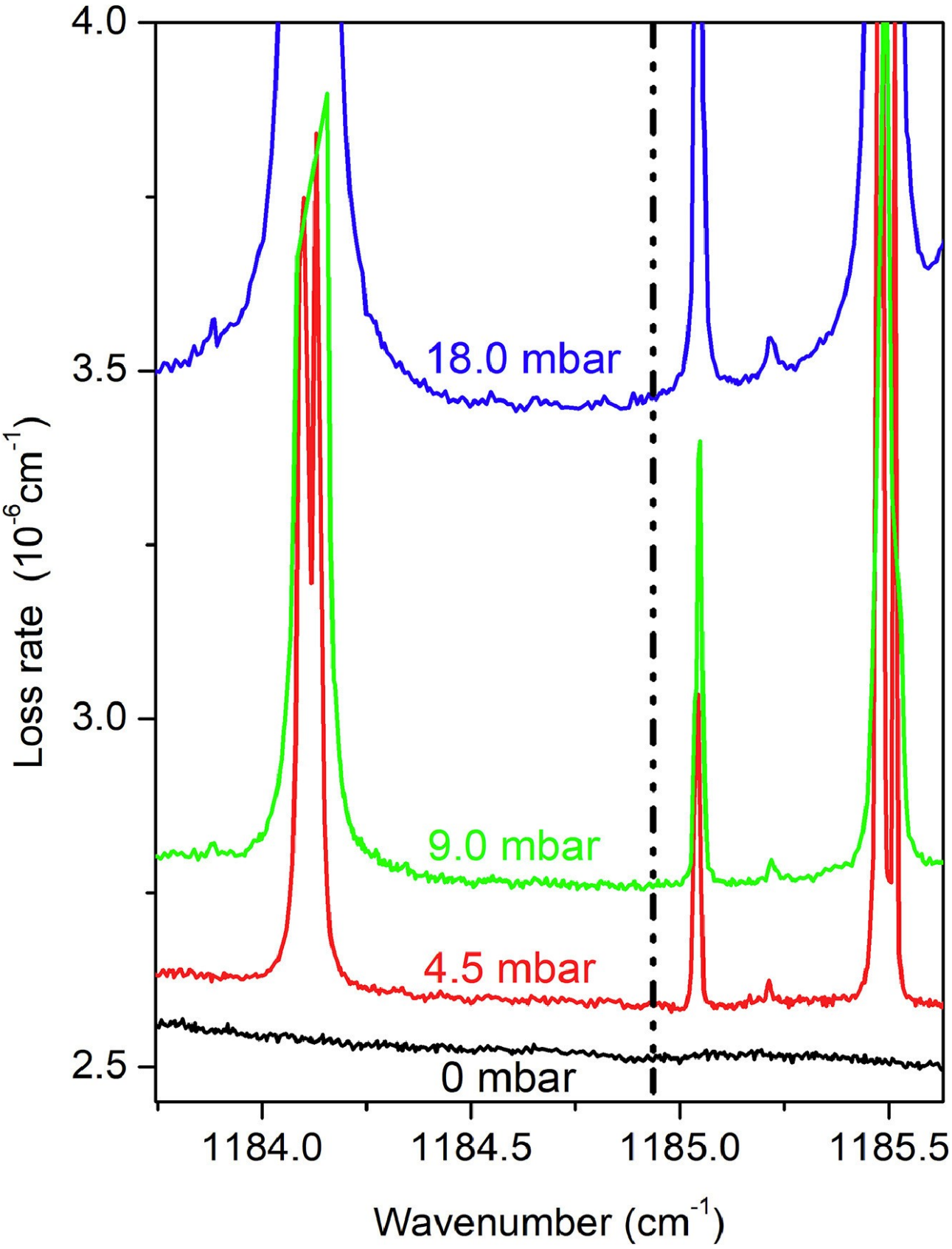

Fig . 5

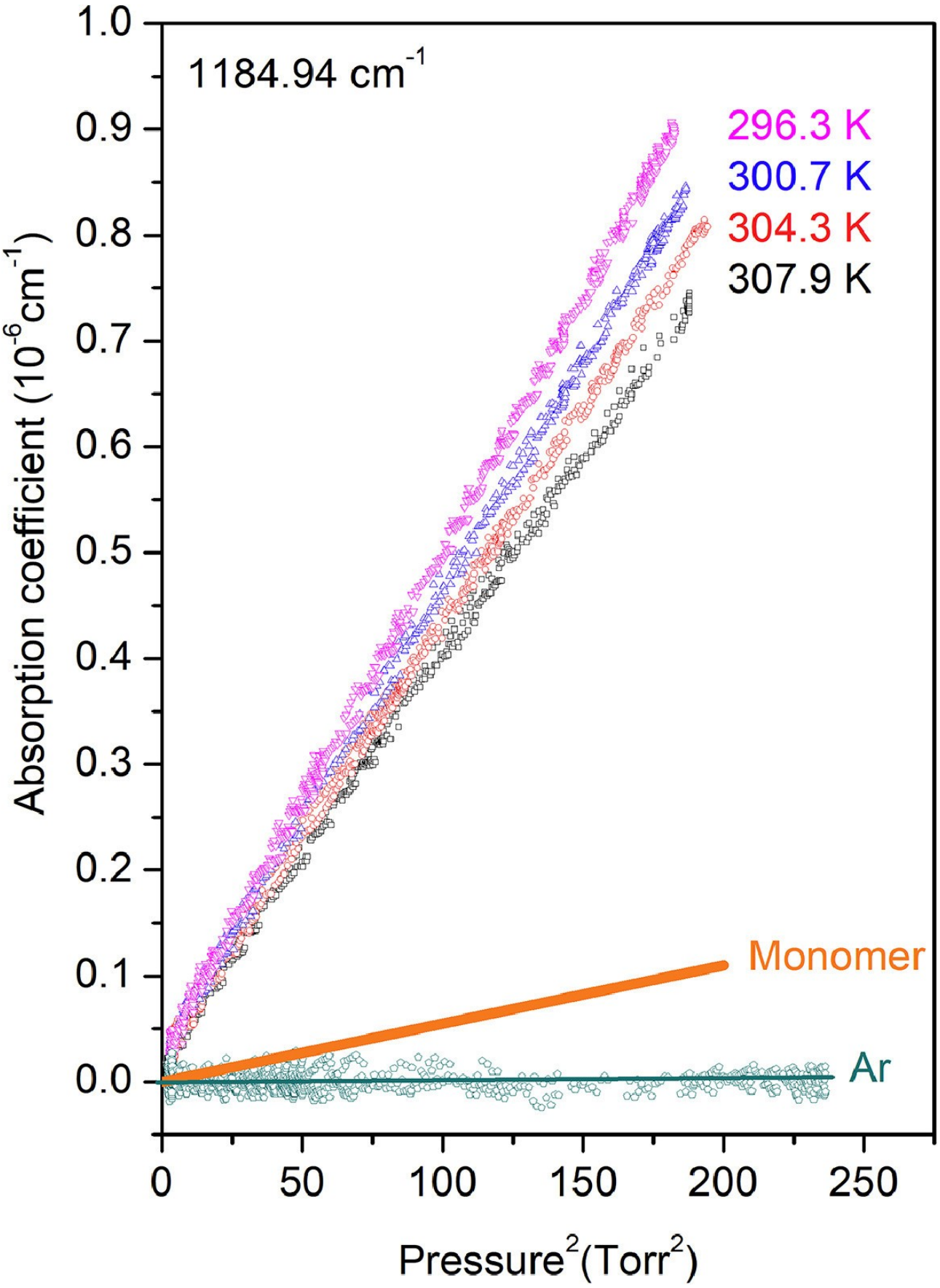

Fig . 6

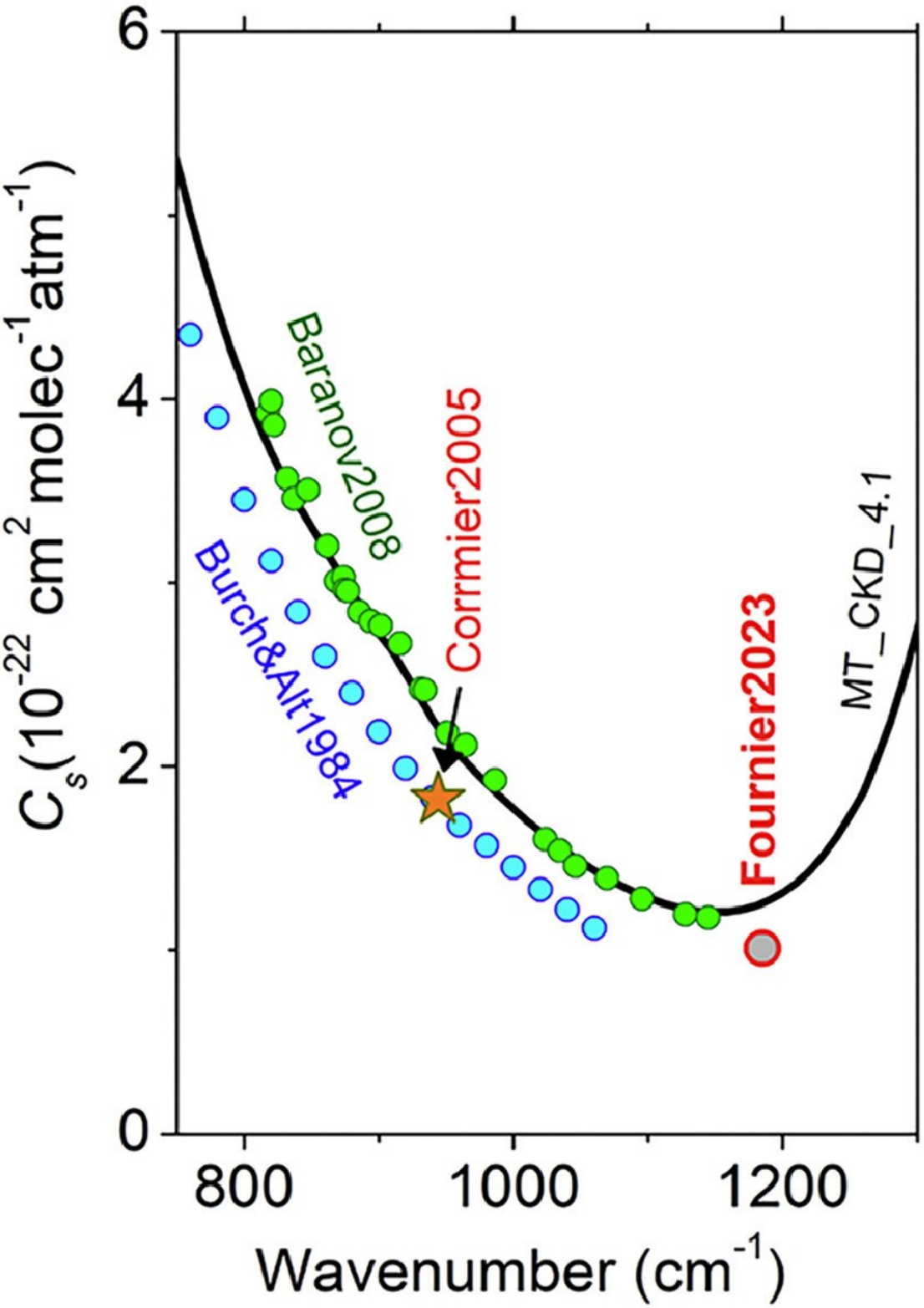

Fig. 7

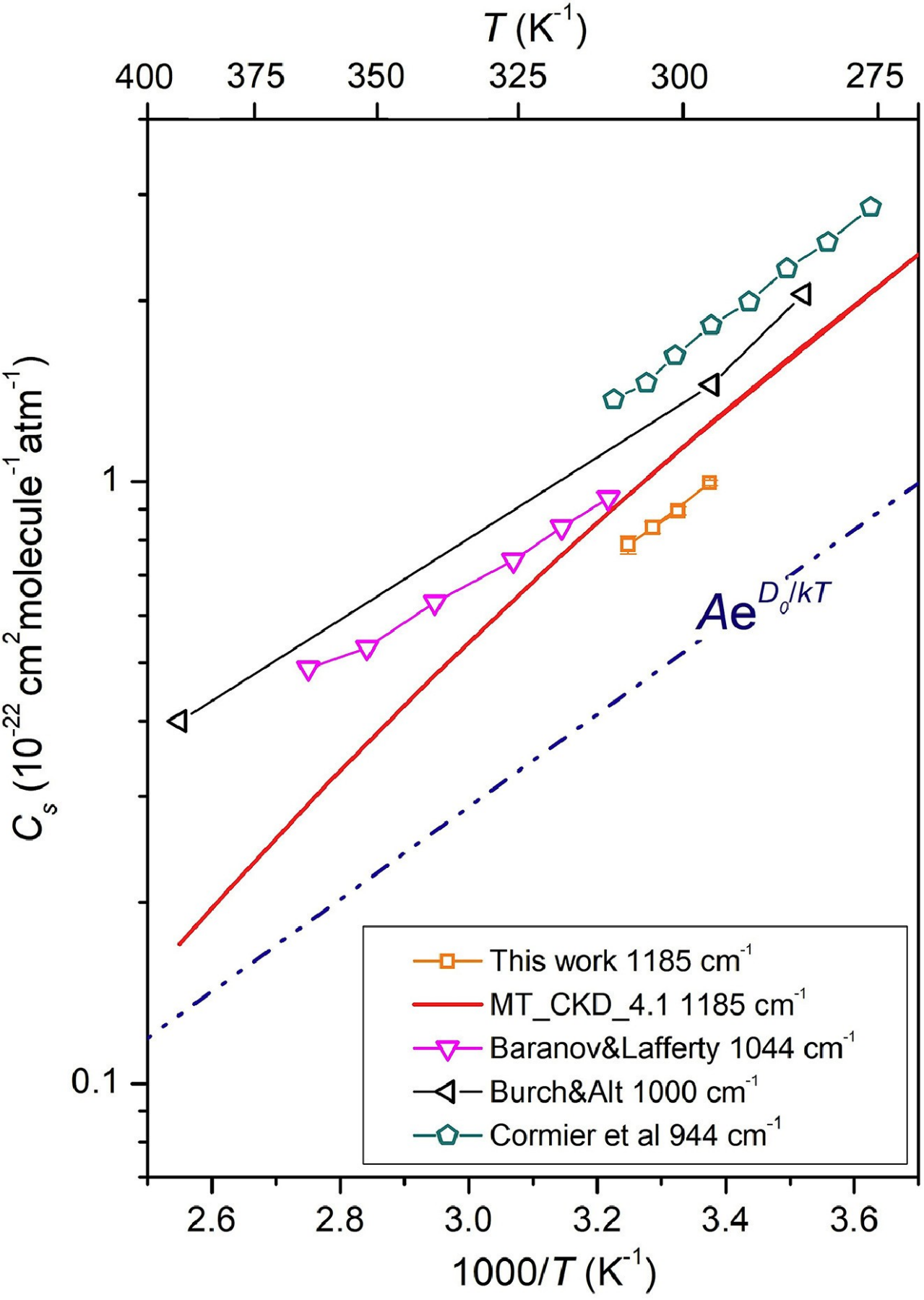

Fig. 8